Supplementary Information

Elliptical nanoantenna arrays plasmonic metasurface for efficient solar energy harvesting

Zahra Ashrafi-Peyman,[a] Amir Jafargholi[b,c] and Alireza Z. Moshfegh*[a,d]

a. *Department of Physics, Sharif University of Technology, Tehran 11555-9161, Iran. E-mail: moshfegh@sharif.edu*
b. *Laboratory of Wave Engineering, School of Electrical Engineering, Swiss Federal Institute of Technology in Lausanne (EPFL), Lausanne, Switzerland.*
c. *Department of Energy Engineering and Physics, Amirkabir University of Technology, Tehran 15875-4413, Iran.*
d. *Center for Nanoscience and Nanotechnology, Institute for Convergence Science & Technology (ICST), Sharif University of Technology, Tehran 11365-8639, Iran.*

Content

Supplementary Section 1: Rising interest in research papers on metasurfaces and solar energy

In the optical sciences, a new class of materials with artificially created nanostructures with pitch sizes much smaller than the wavelengths of electromagnetic (EM) radiation began to draw attention about 20 years ago.[1] In the early stages of metamaterials research, the emphasis was primarily on three-dimensional structures.[2] However, metasurfaces, which are optical antenna periodic arrays with subwavelength dimensions, have recently gained significant attention for their ability to control and manage optical properties at interfaces, making them a key enabler for flat optical components.[3] Metasurfaces, which deal with subwavelength thickness, are artificially engineered two-dimensional (2D) or planar versions of metamaterials that have attracted a great deal of interest concerning solar energy. Based on the Web of Science citation database, Fig. S1 illustrates the continuously rising trend in the number of publications containing the keywords ("solar") AND ("metamaterial*" OR "metasurface*") in the topic (title, abstract, and keywords), demonstrating the significance of this growing active field.

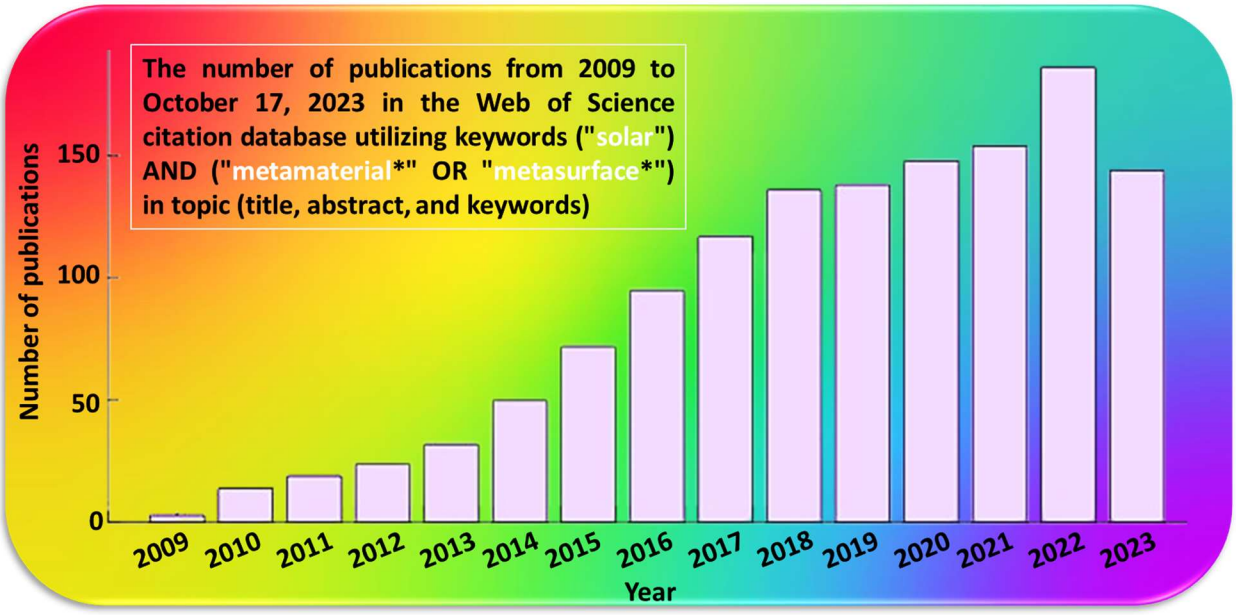

Fig. S1 The number of publications in the Web of Science citation database utilizing keywords ("solar") AND ("metamaterial*" OR "metasurface*") in topic (title, abstract, and keywords). Accessed on October 17, 2023.

Supplementary Section 2: Comparison of the melting points of different materials

In the case of free-standing particles, the general form of $T_{mp}/T_{mb} = 1 - C/D$, where T_{mp} and T_{mb} are the melting points of the nanoparticle and bulk material, respectively, D is the thickness (or diameter) of the nanoparticle, and C is a constant that depends on the modeling parameters, shows how the melting temperatures of nanoparticles fall linearly with decreasing size in relation to the bulk melting temperature.[4,5] The dimensions of metasurfaces[6,7] and the nanostructure suggested in this article are greater than the nanoparticle critical size[8] needed to alter the melting point. Furthermore, nitrides (such as TiN and GaN) can be stable in high-temperature applications, as demonstrated by several experimental studies.[7,9,10]

The comparison of the melting points of the various materials employed in the solar absorbers described in numerous articles shows that, after graphene, tungsten (W), and tantalum (Ta), titanium nitride (TiN) and gallium nitride (GaN) have high melting points compared to other materials and are positioned fairly appropriately for high-temperature applications. Fig. S2 compares the melting points of TiN and GaN with a variety of other materials based on data adapted from Ref. 11.

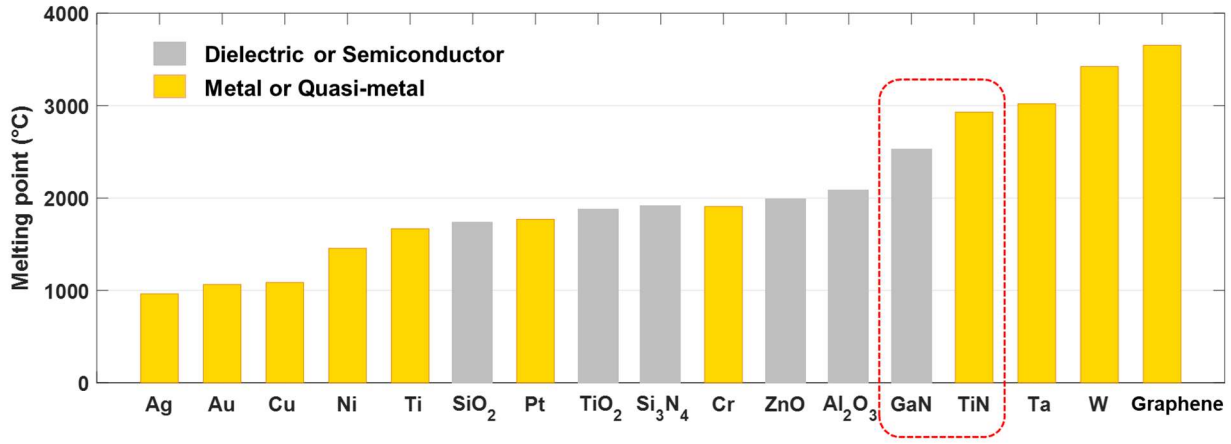

Fig. S2 Comparison of the melting points of applied TiN and GaN in the designed nanostructure with different materials based on data adapted from Ref. 11.

Supplementary Section 3: The design and optimization method of the proposed nanostructure

An illustration of our nanostructure design and optimization method is shown in Fig. S3a and b, which shows the simulated spectra with gradual improvement of the absorption performance. To begin with, we have used a nanostructure consisting of a uniform substrate of TiN and elliptical GaN nanoantennas with a thickness of 70 nm placed on top of it (design 1). This nanostructure provides absorption in the UV region. In the design of the next nanostructure that we simulated, smaller GaN elliptical nanoantennas have been added to it (design 2). As we can see in Fig. S3b, the obtained absorption response is slightly better than the previous design. In the third nanostructure that we examined (design 3), we added a TiN nanoantenna to the nanostructure of design 1, which increased the absorption in the visible and NIR regions, and design 4 is the addition of TiN elliptical nanoantennas to design 2, in which case the absorption of the nanostructure is close to unity in 300–1116 nm of wavelength. Here we have seen a drastic change in absorption response and an improvement in absorption performance.

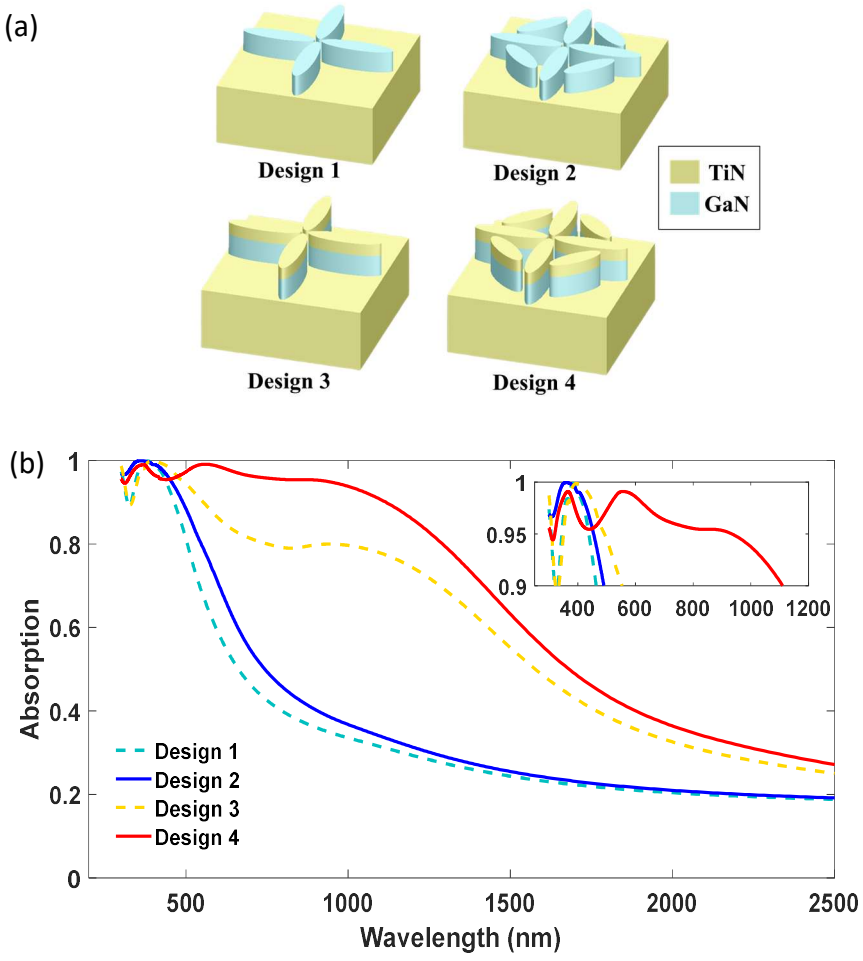

Fig. S3 (a) The design method of the proposed nanostructure and (b) the absorption diagram related to each of the designs. The inset in (b) shows its magnified section.

Supplementary Section 4: Absorption and transmission of a flat TiN layer and Influence of different structural parameters

Absorption and transmission of a flat TiN layer:

Fig. S4a illustrates a flat TiN layer, and Fig. S4b shows the real part (ε_1) and imaginary part (ε_2) of the relative permittivity of TiN material.[12] Additionally, Fig. S4c and Fig. S4d show the absorption and transmission of a flat TiN layer with different thicknesses, respectively. In Fig. S4b, we discover that this material can absorb some incident light up to a wavelength close to 500 nm since the epsilon-near-zero (ENZ) of the TiN material is about at this wavelength and the epsilon is positive before this wavelength. Additionally, since the real part of its epsilon becomes significantly negative at wavelengths longer than around 500 nm, this material is a high reflector in this range, minimizing absorption and transmission in this material layer. The simulation results of a flat TiN layer (Fig. S4c and d) confirm the permittivity diagram of TiN material (Fig. S4b).

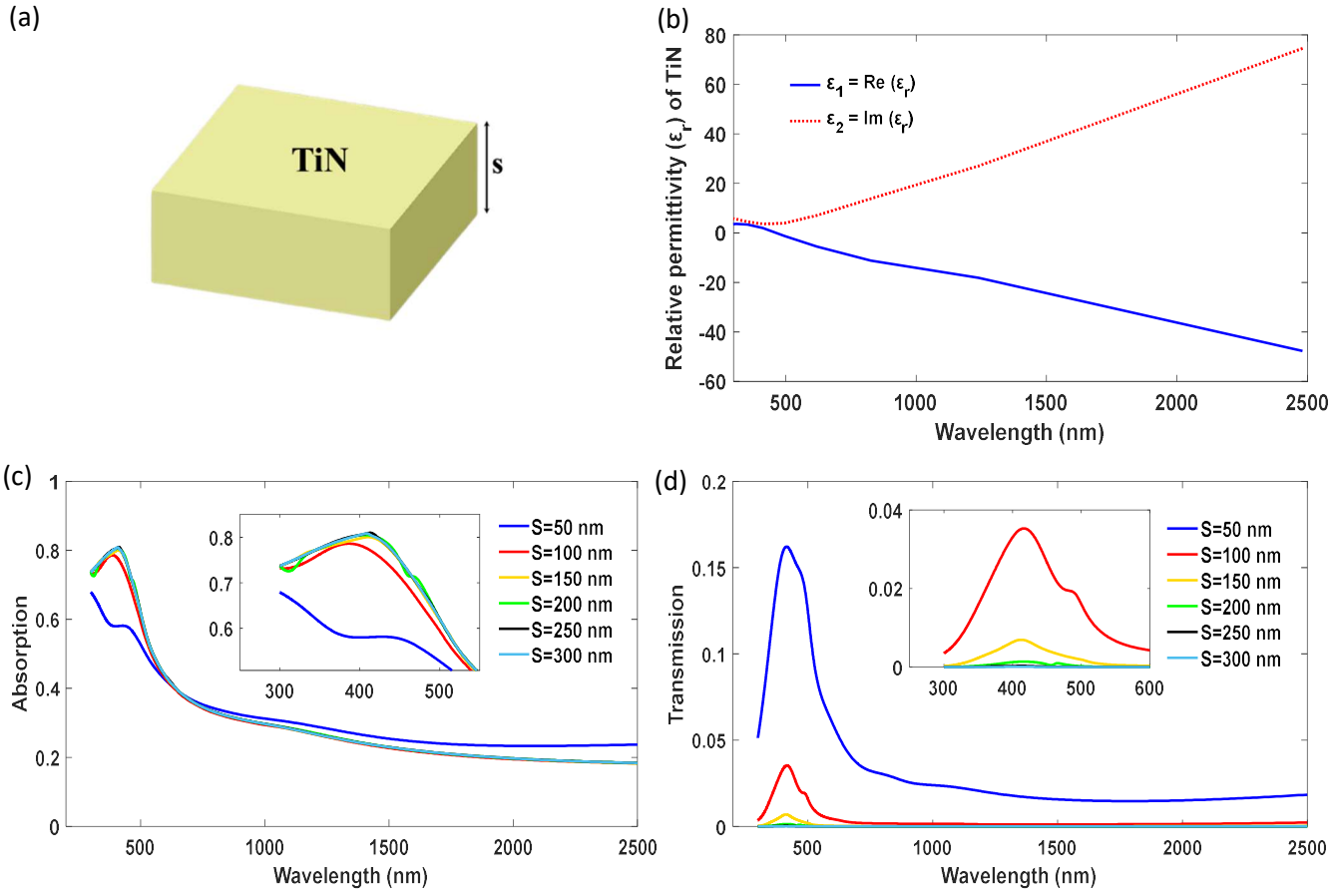

Fig. S4 (a) A flat TiN layer, (b) real and imaginary parts of the relative permittivity of TiN material, (c) absorption and (d) transmission of a flat TiN layer with different thicknesses. The inset in (c) and (d) shows its magnified section.

However, a very thin layer of TiN can somewhat alter how much light is absorbed and transmitted through it. But if the thickness of the layer is greater than 150 nm, there is no significant change between the absorption and transmission spectra. This is because the TiN layer is thicker than the skin depth at which the incident light can penetrate. The skin depth is the depth below a conductor's surface at which the EM wave has attenuated to $1/e$ (about 37% or approximately a third) of its value at the surface. The established equation (S1) can be used to calculate skin depth.[13]

$$\delta = \sqrt{1/\sigma\pi f \mu_0 \mu_r} \quad \text{(S1)}$$

where σ, f, μ_o and μ_r stand for, respectively, the specific conductance of material, frequency of the plan wave, vacuum permeability (12.57×10^{-7} H/m) and relative magnetic permeability of TiN material. In order to prevent incident light from penetrating the proposed absorber, we decided to use a substrate with a 150 nm thickness. It is capable of entirely obstructing light transmission.

Influence of different structural parameters:

By increasing the sweep period from 350 nm to 500 nm in Fig. S5a, we observe a significant reduction in absorption. This reduction in absorption may be caused by an increase in the gap size at the edges of the unit cell boundary as the unit cell size increases, leading to a decrease in the LSPRs. In Fig. S5b, *h* is swept from 50 nm to 90 nm. The absorption increases with the increase of *h* in spectral regions around λ=600 nm and later, while it decreases in the region before λ=600 nm. In Fig. 4c, the absorption broadens and exhibits red shifts when *t* is increased and swept from 10 nm to 100 nm, but *t*=40 nm is chosen in order to reduce the thickness of the nanostructure and the movement of the mean free pass of electrons in the metals. Although when *t* is change, we can achieve broadband absorption or tuneable absorption with different wavelengths. In Fig. S5d, the absorption becomes more widespread as parameter *a* rises; nevertheless, the absorption rate falls for wavelengths prior to 600 nm. The alterations in Fig. S5e are connected to the nanostructure's central gap. As the central gap is increased, the gap at the edges of the unit cell border decreases. The results show that a gap of 15 nm is the best. The minimum gap, or the distance between the large and small elliptical nanoantennas (parameter *d*), has been swept in Fig. S5f, which demonstrates that for a distance of zero, the absorption is wider but less intense, and the nanostructure's absorption is not significantly different from that of 10 to 30 nm of parameter *d*. In Fig. S5g, parameter b_1 is swept from 66 nm to 83.5 nm. The decrease in the parameter b_1 causes the gaps at the unit cell's border edges to get bigger, which in turn causes the absorption to drop. When b_1=83.5 nm, the gaps at the border edges of the unit cell are zero, resulting in a wider but less strong absorption. In Fig. S5h, the absorption becomes more widespread as parameter b_2 rises; nevertheless, the absorption rate falls for wavelengths prior to 600 nm.

It is evident that certain alterations in geometric parameters (for example, 10<*g*<25 nm and 10<*d*<30 nm) exhibit minimal impact on the broad-spectrum absorption capabilities of the proposed metasurface absorber. This observation suggests that the absorber possesses a considerable degree of manufacturing tolerance, simplifying the practical production process for this absorber.

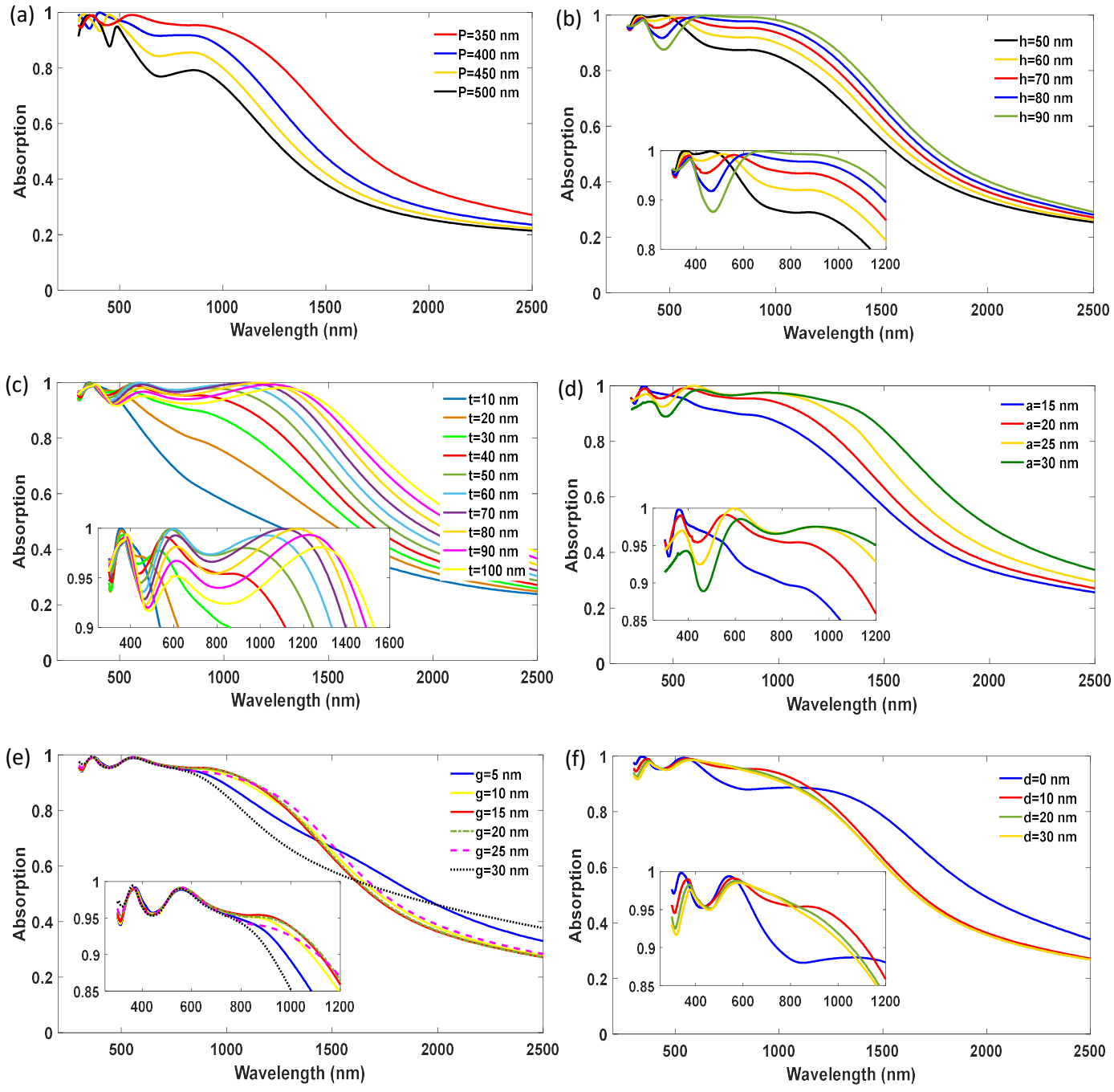

Continued on the next page

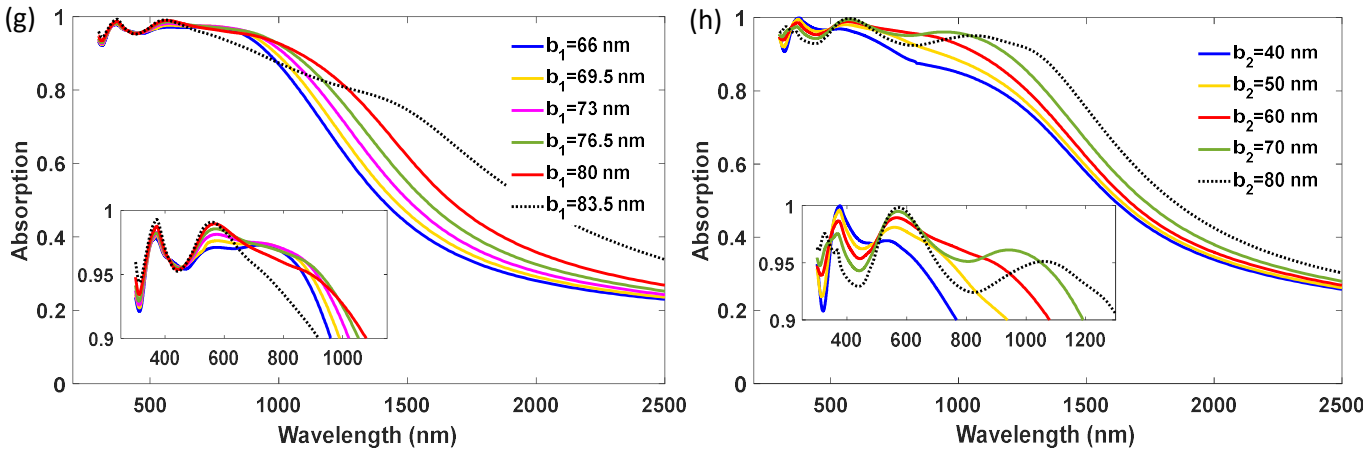

Fig. S5 Absorption spectra of the metasurface absorber with different geometric parameters. (a) period of a unit cell, *P*, (b) thicknesses of GaN elliptical-shaped nanoantenna, *h*, (c) thicknesses of TiN elliptical-shaped nanoantenna, *t*, (d) the minor radius of the nanoantenna, *a*, (e) nanoantenna gap in the center of the nanostructure, *g*, (f) gap or the distance between the large and small elliptical nanoantenna, *d*, (g) major radius of the large elliptical nanoantenna, b_1, and (h) major radius of the small elliptical nanoantenna, b_2. The insets show its magnified section.

Supplementary Section 5: Electric field distribution in the proposed nanostructure

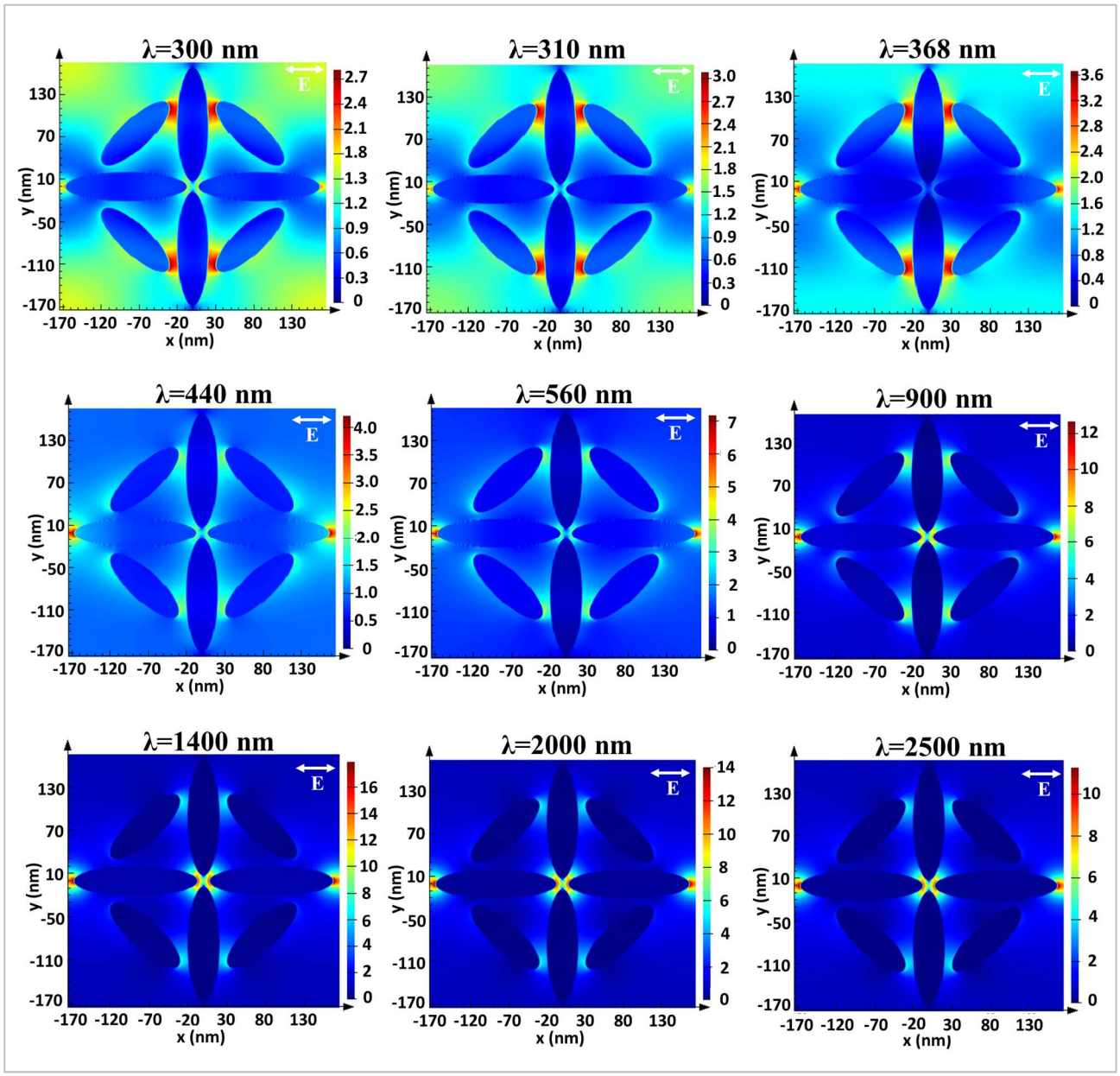

Fig. S6 Electric field distribution ($|E|/|E_0|$) in the xy plane and in the center of the TiN elliptical nanoantennas under TM polarization excitation at different wavelengths.

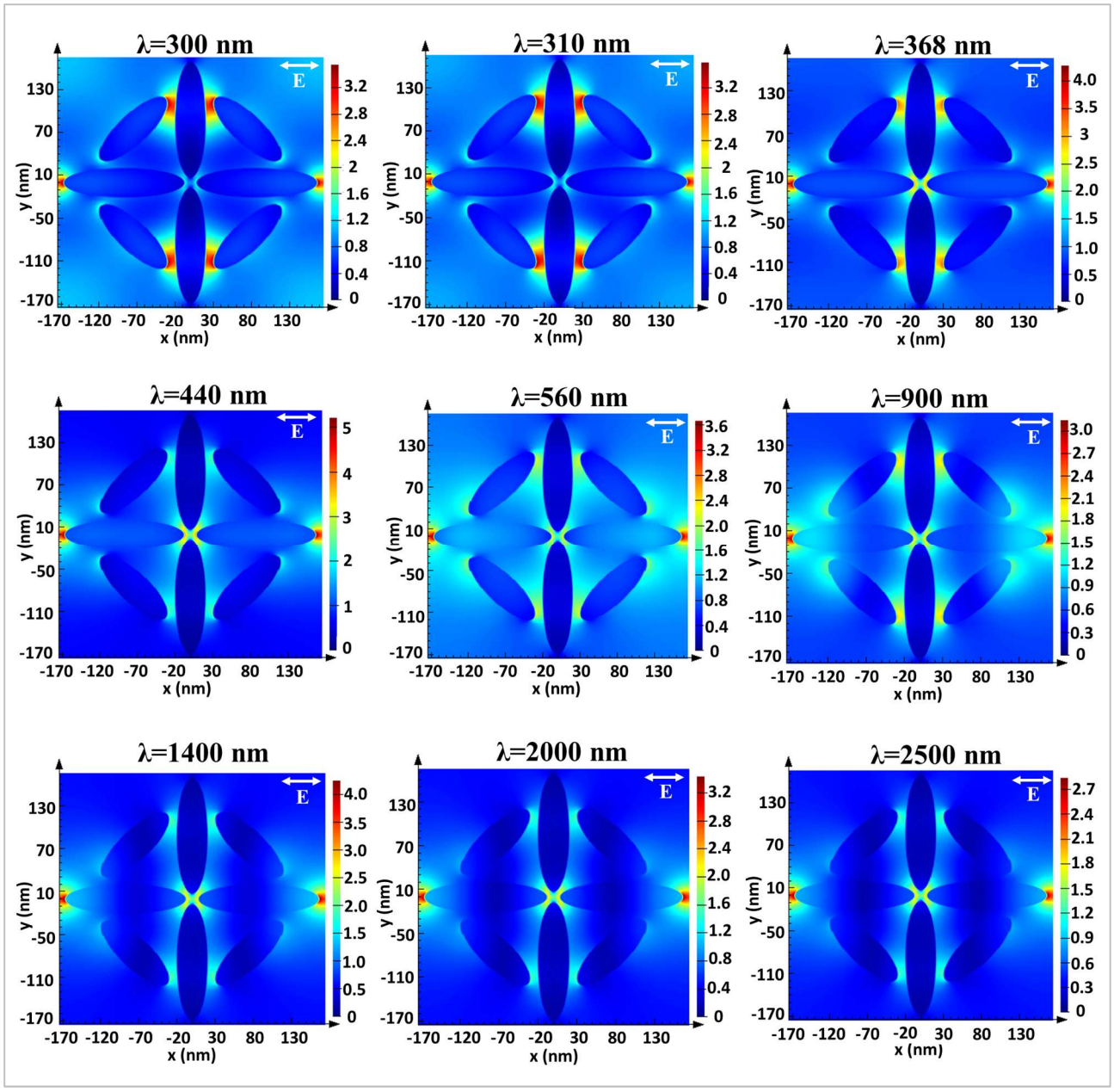

Fig. S7 Electric field distribution ($|E|/|E_0|$) in the xy plane and in the center of the GaN elliptical nanoantennas under TM polarization excitation at different wavelengths.

Supplementary Section 6: Effects of incident angle and polarization of the light

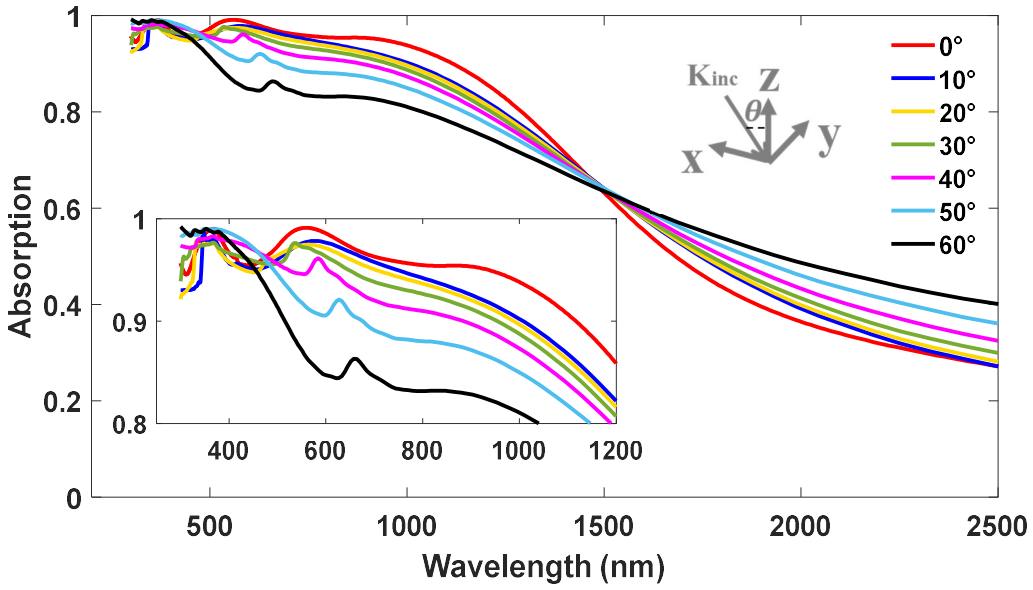

Fig. S8 Absorption spectra of the absorber with six different incident angles (θ). The inset shows its magnified section.

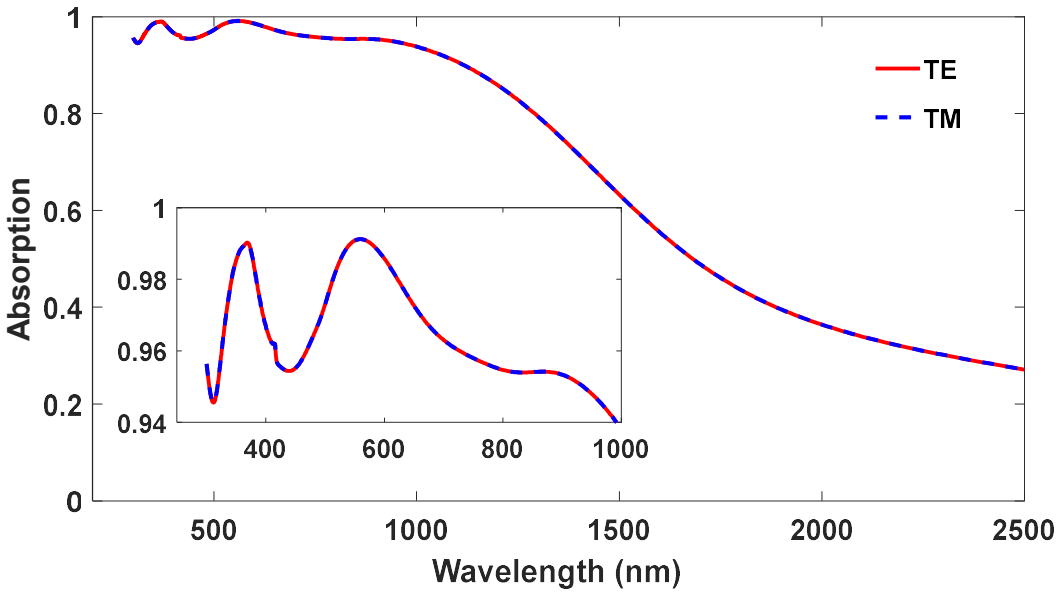

Fig. S9 Absorption spectra of the proposed absorber with TM and TE polarizations. The inset shows its magnified section.

Supplementary Section 7: Analysis in water

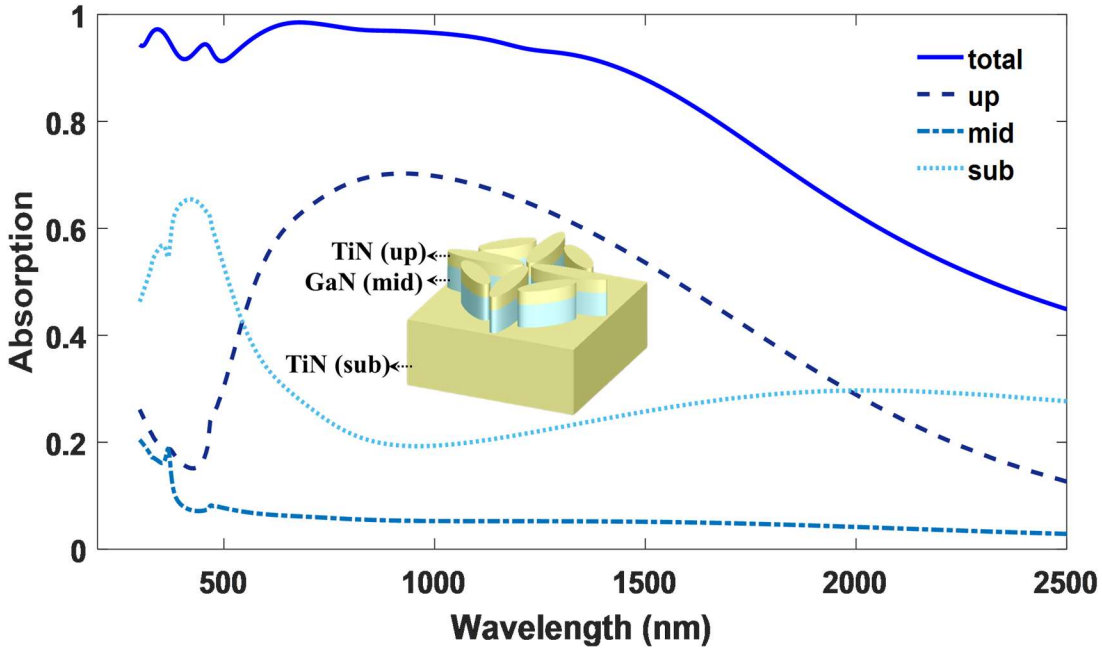

Fig. S10 Absorption spectrum in different parts of the proposed nanostructure in the water environment.

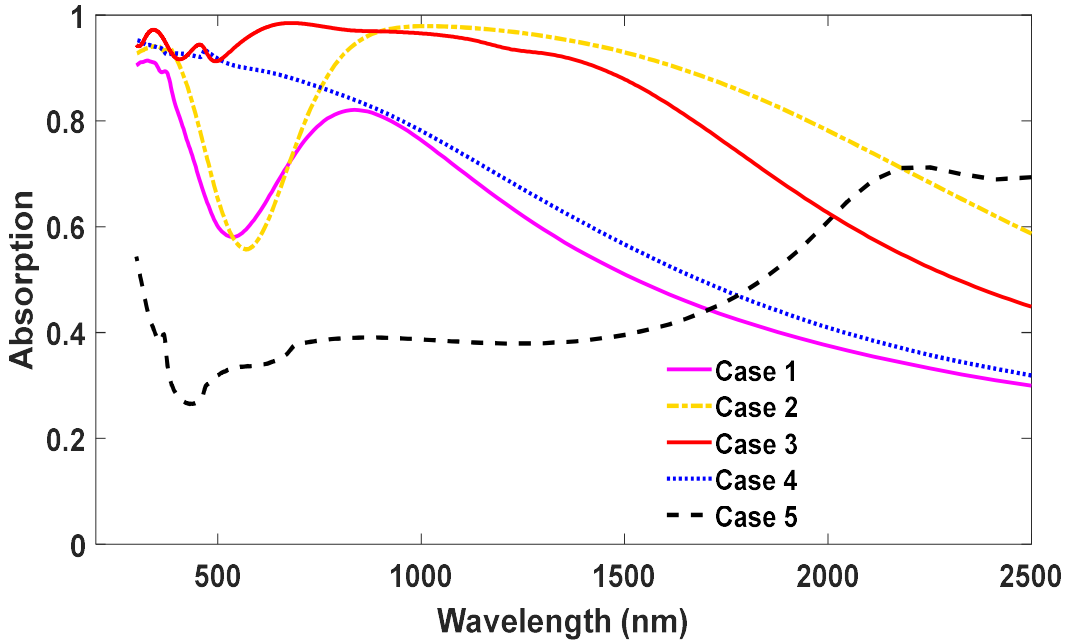

Fig. S11 Absorption spectra of nanostructures associated with cases 1 to 5 submerged in water (For cases 1 to 5, please see Fig. 8a).

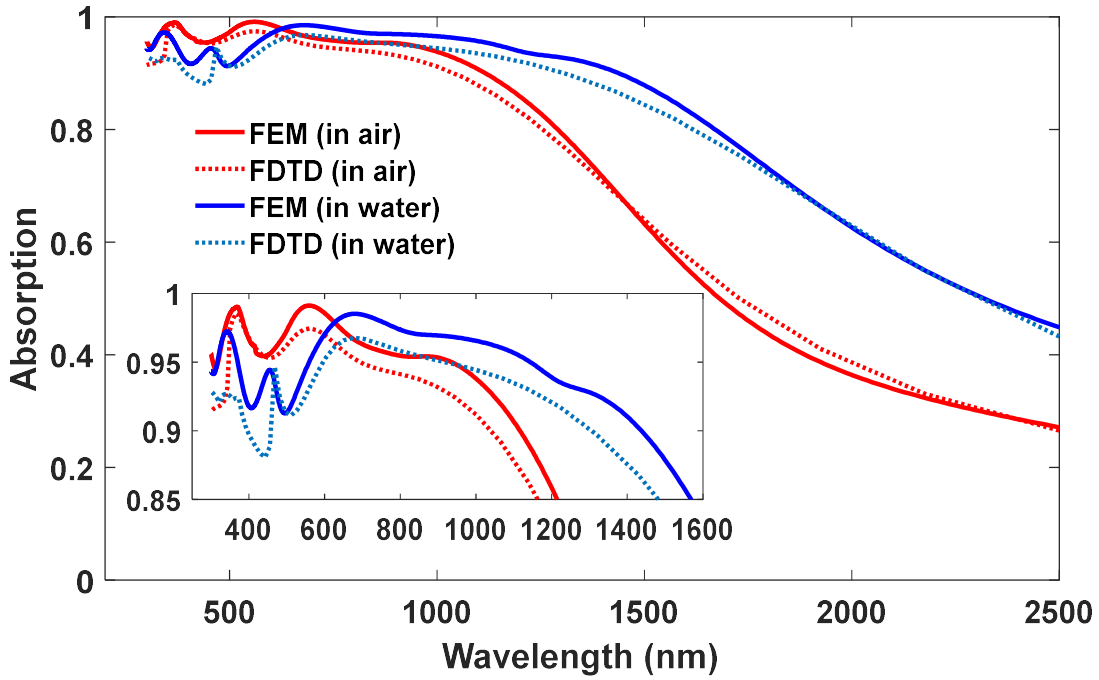

Fig. S12 Confirmation of the reliability and precision of FDTD and FEM models for absorption of the proposed nanostructure in the air and water environments. The inset shows its magnified section.

Supplementary Section 8: Comparison of the proposed nanostructure with recent works

Table S1. Structural factors and performance of the designed nanostructure absorber with those of similar recent works.

Structure type	Material	Thickness (nm)	The operating region of absorption more than 90% (nm)	Sim./Exp.	Reference
Metallic nanoparticle arrays	Au/SiO_2	147	450-525 & 585-820	Sim./Exp.	[14]. Z. Liu, et al., ACS Appl. Mater. Interfaces 2015
(W NP arrays in a SiO_2 layer) on alternating SiO_2/W layers	SiO_2/W	745	350-1680	Sim.	[15]. D. Wu, et al., Sol. RRL 2017
2D gratings	$CuBi_2O_4/SiO_2/Ag$	200	450-650	Sim.	[16]. P. Manley, et al., ACS Appl. Energy Mater. 2018
Shapes of holes and trenches/ square holes	Graphene metamaterial (RGO/Dielectric layer)/Cu	1030	280-1500	Sim./Exp.	[17]. K.-T. Lin, et al., Nat. Commun. 2020
Disk and cuboid	$Ti/W/SiO_2/Au$	450	200-1959	Sim.	[18]. P. Yu, et al., Renew. Energ. 2020
Ring-disc	W/SiO_2	300	420-1950	Sim.	[19]. Z. Yi, et al., Nanoscale 2020
Circular and elliptical disk	W/Monolayer $MoS_2/SiO_2/Fe$	660	280-2030	Sim.	[20]. J. Li, et al., Mater. Today Energy. 2020
Three-layer disk	SiO_2/TiN/Ti/Au	650	516-2696	Sim./Exp.	[21]. F. Qin, et al., Sol. Energy Mater. Sol. Cells. 2020
Elliptical rings-shaped fractal structure	W/SiO_2/Perfect electric conductor (PEC)	135	400-750	Sim.	[22]. R. Bilal, et al., Sci. Rep. 2020
Nanocubes	ZnO/Cu/Au	240	270-600	Sim./Exp.	[23]. J. Y. Y. Loh, et al., Nano Lett. 2021
TiN nanodisk arrays	TiN	160	400-780	Sim./Exp.	[24]. M.-J. Yu, et al., ACS Photonics 2021
Nanopillar arrays	CdS/Pt/Ni	435	300-1100	Sim./Exp.	[25]. R. Yalavarthi, et al., ACS Appl. Energy Mater. 2021
Nanohole array	$Pt/TiO_2/Au$	75	400-450	Sim./Exp.	[26]. H. Jia, et al., ACS Photonics 2022
Eight spoked asterisk	$Au/Graphene/SiO_2$	3200	200-750	Sim.	[27]. S. K. Patel, et al., Renew. Energ. 2022
Circular holes (nanopillar embedded in nanohole)	MgF_2/TiO_2/TiN/PMMA	370	300-1500	Sim./Exp.	[28]. Q. Qian, et al., Nanoscale 2022

Notched nanoring	$Ni/SiO_2/Au$	410	300-2400	Sim.	[29]. Z. Wang, et al., Sol. Energy. 2022
Cylinder array	TiN/SiO_2	825	250-1750	Sim.	[30]. B. Yang, et al., Int. J. Therm. Sci. 2023
Crosses	Cr/SiO_2	260	300-1200	Sim./Exp.	[31]. A. S. Rana, et al., Renew. Sustain. Energy Rev. 2023
Multilayer structure	TiN/SiO_2	525	300-450 & 600-2500	Sim.	[32]. H. Liu, et al., Phys. Chem. Chem. Phys. 2023
Multilayer nanodisk	$TiN/Si_3N_4/W$	780	280–3209	Sim.	[33]. Y. Zheng, et al., Appl. Therm. Eng. 2023
Elliptical nanoantenna arrays	TiN/GaN	260	300-1116 (in air) 300-1436 (in water)	Sim.	Proposed nanostructure

Supplementary Section 9: Cut-off wavelengths of ideal solar absorbers at several temperatures

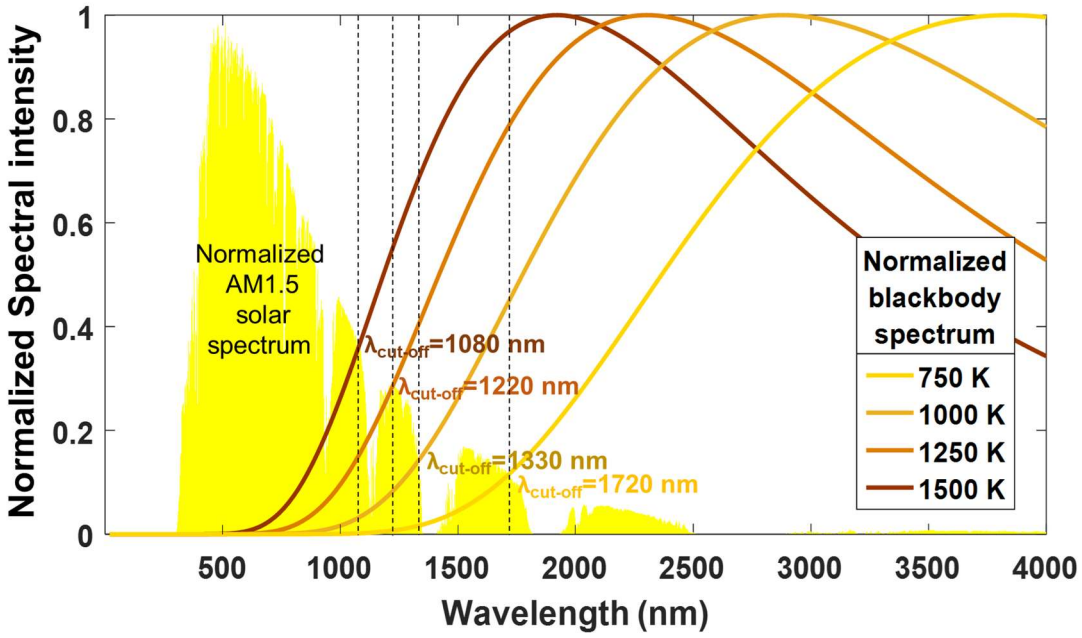

Fig. S13 Normalized spectral intensities of the AM1.5 solar spectrum and the blackbody radiation spectra at different temperatures of 750, 1000, 1250, and 1500 K. The ideal solar absorber has cut-off wavelengths at 1720, 1330, 1220, and 1080 nm, respectively.

Supplementary Section 10: Comparison of our work outcomes and the experimental and theoretical outcomes of Hu's article[34]

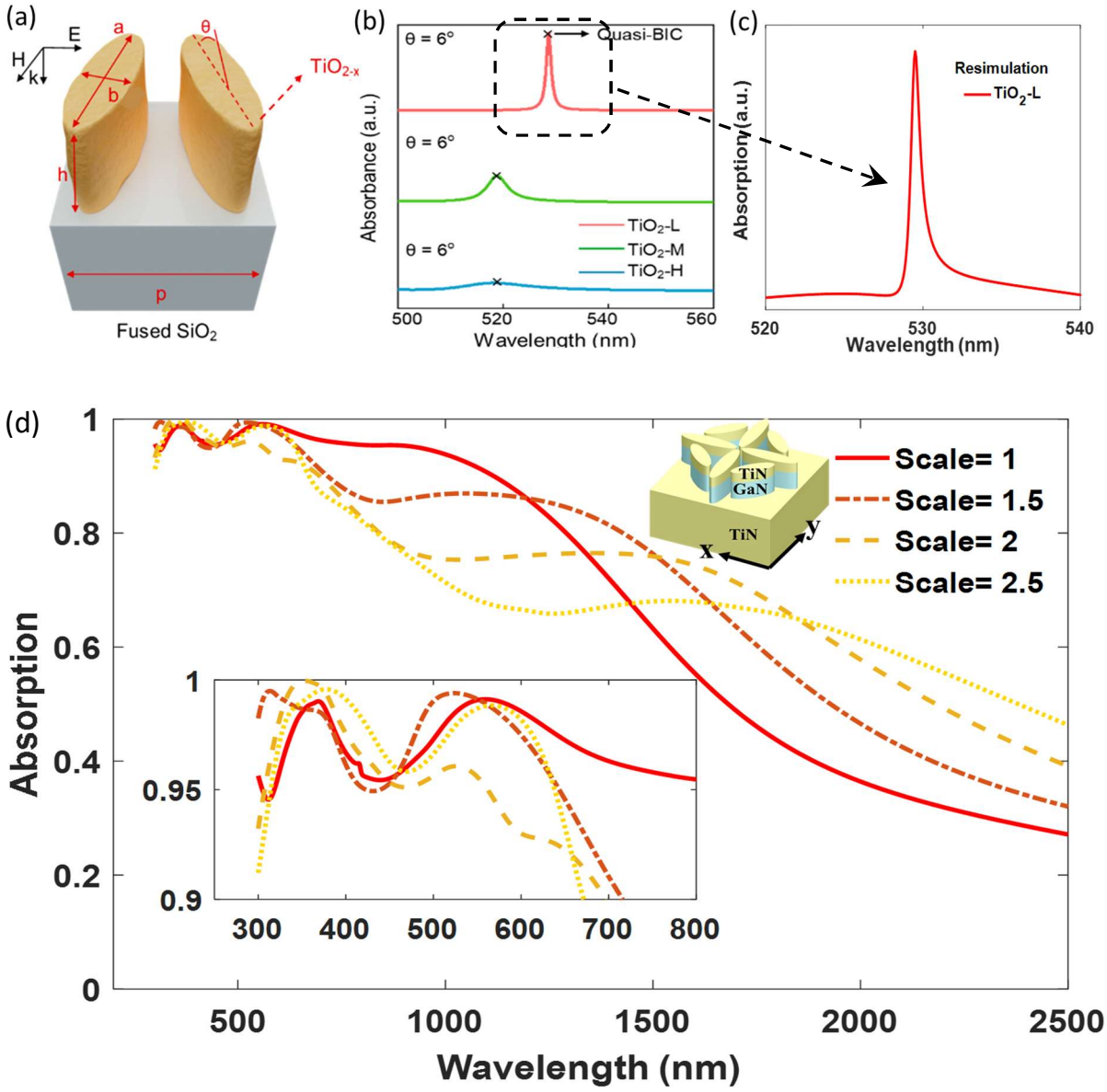

Fig. S14 (a) Sketch of a TiO_{2-x} BIC unit cell with tilting angle θ in Hu's article[34]. The geometrical parameters of the unit cell are *a*=274 nm, *b*=103 nm, *h*=100 nm, and *p*=331 nm (b) Absorbance spectra of BIC metasurfaces composed of different TiO_{2-x} materials with a tilting angle of θ=6°. In Hu's article, TiO_{2-x} are denoted as TiO_2-L, TiO_2-M, and TiO_2-H for the lowest, moderate, and highest oxygen vacancy concentrations, respectively. (c) A resimulation of one of the results of Hu's article shows the high agreement of our simulation with the results of this article. (d) Optical absorption of our proposed nanostructure, which employs various scales along the x and y axes. The inset in (d) shows its magnified section. Figures adapted with permission from: (a, b) Ref. 34. Copyright 2022 American Chemical Society.

References

1 E. Cortés, F. J. Wendisch, L. Sortino, A. Mancini, S. Ezendam, S. Saris, L. de S. Menezes, A. Tittl, H. Ren and S. A. Maier, *Chemical Reviews*, 2022, **122**, 15082-15176.

2 C. M. Soukoulis and M. Wegener, *Nature Photonics*, 2011, **5**, 523-530.

3 F. Ding, A. Pors and S. I. Bozhevolnyi, *Reports on Progress in Physics*, 2017, **81**, 026401.

4 A. Safaei, M. A. Shandiz, S. Sanjabi and Z. Barber, *The Journal of Physical Chemistry C*, 2008, **112**, 99-105.

5 J. Zhu, Q. Fu, Y. Xue and Z. Cui, *Journal of Materials Science*, 2016, **51**, 4462-4469.

6 C.-C. Chang, W. J. Kort-Kamp, J. Nogan, T. S. Luk, A. K. Azad, A. J. Taylor, D. A. Dalvit, M. Sykora and H.-T. Chen, *Nano Letters*, 2018, **18**, 7665-7673.

7 W. Li, U. Guler, N. Kinsey, G. V. Naik, A. Boltasseva, J. Guan, V. M. Shalaev and A. V. Kildishev, *Advanced Materials*, 2014, **26**, 7959-7965.

8 P. Antoniammal and D. Arivuoli, *Journal of Nanomaterials*, 2012, **2012**, 8-8.

9 T. Krekeler, S. S. Rout, G. V. Krishnamurthy, M. Störmer, M. Arya, A. Ganguly, D. S. Sutherland, S. I. Bozhevolnyi, M. Ritter and K. Pedersen, *Advanced Optical Materials*, 2021, **9**, 2100323.

10 J. Liang, A. Kobayashi, Y. Shimizu, Y. Ohno, S. W. Kim, K. Koyama, M. Kasu, Y. Nagai and N. Shigekawa, *Advanced Materials*, 2021, **33**, 2104564.

11 D. R. Lide, *CRC Handbook of Chemistry and Physics*, CRC Press, 2004.

12 Refractive Index Database, https://refractiveindex.info/?shelf=main&book=TiN&page=Pfluger, accessed October 30, 2023.

13 R. B. Keller, *Design for Electromagnetic Compatibility--In a Nutshell: Theory and Practice*, Springer Nature, 2023.

14 Z. Liu, X. Liu, S. Huang, P. Pan, J. Chen, G. Liu and G. Gu, *ACS Applied Materials & Interfaces*, 2015, **7**, 4962-4968.

15 D. Wu, Y. Liu, Z. Xu, Z. Yu, L. Yu, L. Chen, C. Liu, R. Li, R. Ma and J. Zhang, *Solar Rrl*, 2017, **1**, 1700049.

16 P. Manley, F. F. Abdi, S. Berglund, A. N. Islam, S. Burger, R. van de Krol and M. Schmid, *ACS Applied Energy Materials*, 2018, **1**, 5810-5815.

17 K.-T. Lin, H. Lin, T. Yang and B. Jia, *Nature Communications*, 2020, **11**, 1389.

18 P. Yu, H. Yang, X. Chen, Z. Yi, W. Yao, J. Chen, Y. Yi and P. Wu, *Renewable Energy*, 2020, **158**, 227-235.

19 Z. Yi, J. Li, J. Lin, F. Qin, X. Chen, W. Yao, Z. Liu, S. Cheng, P. Wu and H. Li, *Nanoscale*, 2020, **12**, 23077-23083.

20 J. Li, X. Chen, Z. Yi, H. Yang, Y. Tang, Y. Yi, W. Yao, J. Wang and Y. Yi, *Materials Today Energy*, 2020, **16**, 100390.

21 F. Qin, X. Chen, Z. Yi, W. Yao, H. Yang, Y. Tang, Y. Yi, H. Li and Y. Yi, *Solar Energy Materials and Solar Cells*, 2020, **211**, 110535.

22 R. Bilal, M. Saeed, P. Choudhury, M. Baqir, W. Kamal, M. M. Ali and A. A. Rahim, *Scientific Reports*, 2020, **10**, 14035.

23 J. Y. Loh, M. Safari, C. Mao, C. J. Viasus, G. V. Eleftheriades, G. A. Ozin and N. P. Kherani, *Nano Letters*, 2021, **21**, 9124-9130.

24 M.-J. Yu, C.-L. Chang, H.-Y. Lan, Z.-Y. Chiao, Y.-C. Chen, H. W. Howard Lee, Y.-C. Chang, S.-W. Chang, T. Tanaka and V. Tung, *ACS Photonics*, 2021, **8**, 3125-3132.

25 R. Yalavarthi, L. Mascaretti, Z. A. Kudyshev, A. Dutta, S. Kalytchuk, R. Zboril, P. Schmuki, V. M. Shalaev, S. Kment and A. Boltasseva, *ACS Applied Energy Materials*, 2021, **4**, 11367-11376.

26 H. Jia, Z. Li, B. Wang, G. Xing, Y. L. Wong, H. Ren, M. Li, K.-Y. Wong, D. Lei and L.-W. Wong, *ACS Photonics*, 2022, **9**, 652-663.

27 S. K. Patel, J. Parmar and V. Katkar, *Renewable Energy*, 2022, **191**, 47-58.

28 Q. Qian, P. Sun, C. Zhang, T. Liu, H. Chen, F. Li, L. Cheng, L. Zhao, X. Li and C. Wang, *Nanoscale*, 2022, **14**, 14801-14806.
29 Z. Wang, Z. Liu, C. Zhang, D. Yang, P. Cheng and Y. Shuai, *Solar Energy*, 2022, **243**, 153-162.
30 B. Yang, Y. Zou, K. Zhou, H. Liu and X. Wu, *International Journal of Thermal Sciences*, 2023, **192**, 108428.
31 A. S. Rana, M. Zubair, Y. Chen, Z. Wang, J. Deng, M. T. S. Chani, A. Danner, J. Teng and M. Q. Mehmood, *Renewable and Sustainable Energy Reviews*, 2023, **171**, 113005.
32 H. Liu, K. Yu, K. Zhang, Q. Ai, M. Xie and X. Wu, *Physical Chemistry Chemical Physics*, 2023, **25**, 10628-10634.
33 Y. Zheng, Z. Yi, L. Liu, X. Wu, H. Liu, G. Li, L. Zeng, H. Li and P. Wu, *Applied Thermal Engineering*, 2023, **230**, 120841.
34 H. Hu, T. Weber, O. Bienek, A. Wester, L. Hüttenhofer, I. D. Sharp, S. A. Maier, A. Tittl and E. Cortés, *ACS Nano*, 2022, **16**, 13057-13068.